ELSEVIER

Journal of Nuclear Materials 252 (1998) 98–109

journal of nuclear materials

Modeling of chemical interactions of fuel rod materials at high temperatures
I. Simultaneous dissolution of UO_2 and ZrO_2 by molten Zr in an oxidizing atmosphere

M.S. Veshchunov *, A.V. Berdyshev

Nuclear Safety Institute (IBRAE), Russian Academy of Science B. Tulskaya, 52, 113191 Moscow, Russia

Received 5 May 1997; accepted 4 September 1997

Abstract

Investigations and modeling of high-temperature processes associated with the oxidation of U–Zr–O molten mixtures under various conditions of severe accidents (intact heated fuel rods or relocating melt) are presented on the basis of a thorough analysis of metallographic post-test examination data obtained in the fuel bundle CORA experiments. In Part I a model of simultaneous dissolution of solid UO_2 and ZrO_2 phases by molten Zr in an oxidizing atmosphere (steam) is presented. This modeling is performed on the basis of the generalization of a previously developed model of UO_2 dissolution by molten Zr taking into account the chemical dissolution by convectively stirring melt of a ZrO_2 layer interacting with steam. The model describes the complicated kinetics of these interactions accompanied by precipitation of a ceramic (U, Zr)O_{2-x} phase in the bulk of the liquid. This process finally leads to complete conversion of the melt into the (U, Zr)O_{2-x} layer located between UO_2 fuel and ZrO_2 shell. Such a three-layer structure was regularly observed in the CORA post-test metallographic examinations of fuel rods heated above the melting point of Zr cladding ($T \geq 1950$°C).

1. Introduction

The previously developed model for UO_2 dissolution by molten Zircaloy (Zry) [1,2] was based on the analysis of UO_2 crucible tests [3–6] performed in an inert atmosphere and for this reason assumed zero mass fluxes at the melt surface opposite to fuel. In a more realistic situation of fuel-cladding interactions in the reactor bundle under conditions of severe accidents at temperatures above the melting point of the α-Zr(O) phase ($T_m \approx 1850$°C), molten metal cladding is located between the UO_2 pellet and the ZrO_2 cladding scale and dissolves these solid materials simultaneously. In the steam atmosphere, dissolution of the ZrO_2 scale is competitive with the molten Zr oxidation which leads to an increase of the ZrO_2 scale thickness and provides additional oxygen flux into the molten phase.

Available experimental data [7] on the ZrO_2 crucible wall dissolution by molten Zry demonstrate that ZrO_2 dissolution rates at high temperatures ($T \geq 1900$°C) are significant and comparable with the UO_2 dissolution rates measured in the analogous crucible tests [3]. For this reason, in the rod geometry neither of these two dissolution processes can be neglected, therefore, their self-consistent consideration seems to be extremely important.

This problem becomes especially complicated since up to now no separate-effect tests on simultaneous dissolution of solid UO_2 and ZrO_2 phases by molten Zr were performed. In this situation only results of post-test metallographic examinations of the fuel rods obtained in the integral experiments can provide some information on the fuel-cladding interactions at high temperatures.

In order to get this information a thorough analysis of

* Corresponding author. Tel.: +7-095 952 2421; fax: +7-095 958 0040; e-mail: vms@ibrae.ac.ru.

0022-3115/98/$19.00
PII S0022-3115(97)00283-3

available data on the CORA tests (FZK, Karlsruhe) was performed paying special attention to recent data on CORA-W1 and CORA-W2 tests since they were described in more detail. Despite using Zr–1% Nb with slightly different properties, these tests provide detailed qualitative and quantitative data on post-test metallographic examinations of the fuel rods [8–10] which allow generalization of the theoretical approach developed in Refs. [1,2] for the modeling of simultaneous dissolution of UO_2 pellets and ZrO_2 scales by molten Zr.

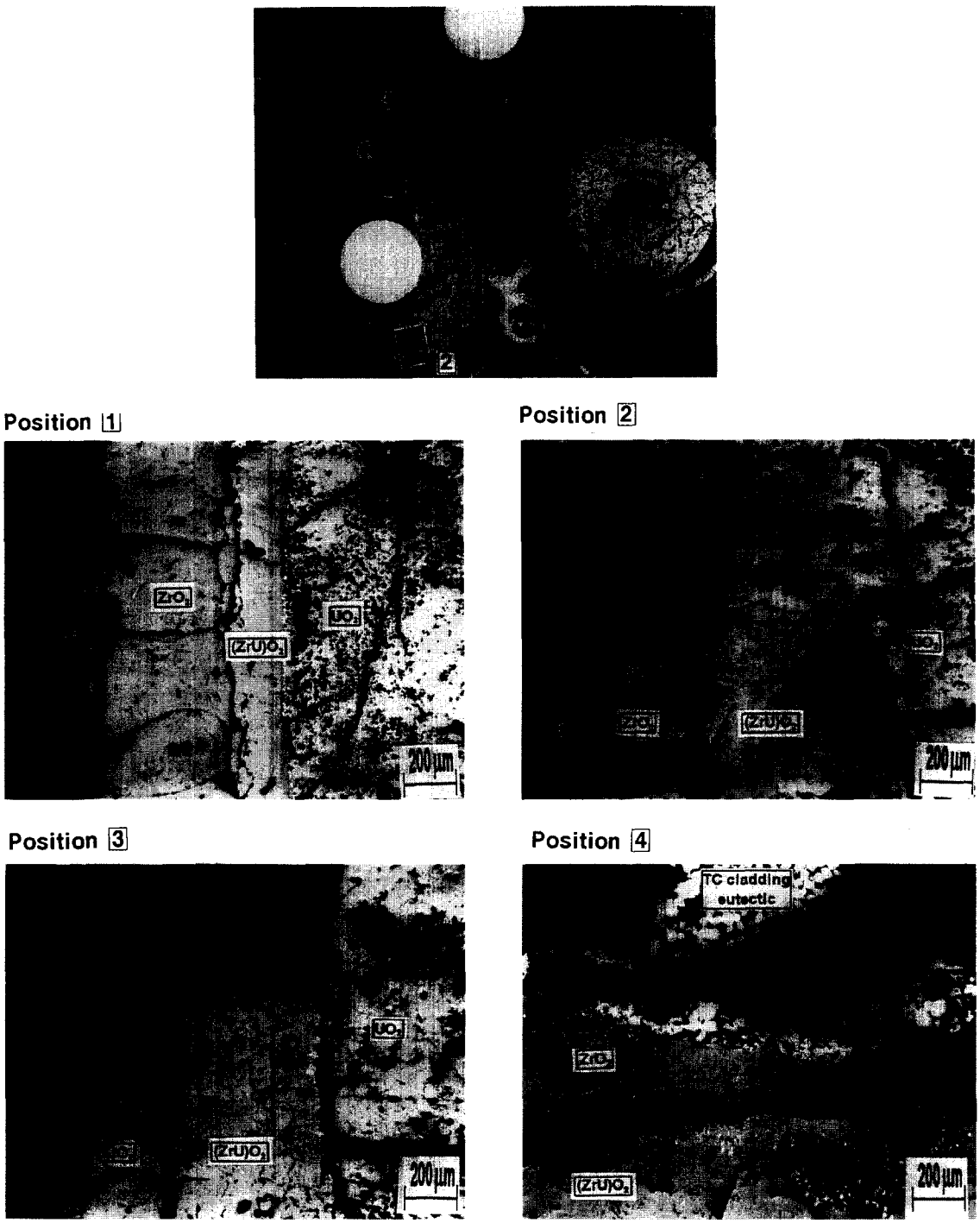

Fig. 1. Cross-section W2-03 of the CORA-W2 test bundle (elevation 327 mm) (from Ref. [10]).

2. Analysis of experimental data

Numerous photographs of various cross-sections of fuel bundles obtained in the CORA-W1 and CORA-W2 tests [8–10] demonstrate that the final product of the simultaneous dissolution of UO_2 and ZrO_2 by molten Zr cladding is the ceramic (U, Zr)O_{2-x} phase (Figs. 1 and 2). Metallographic examinations of the bundle cross-sections at differ-

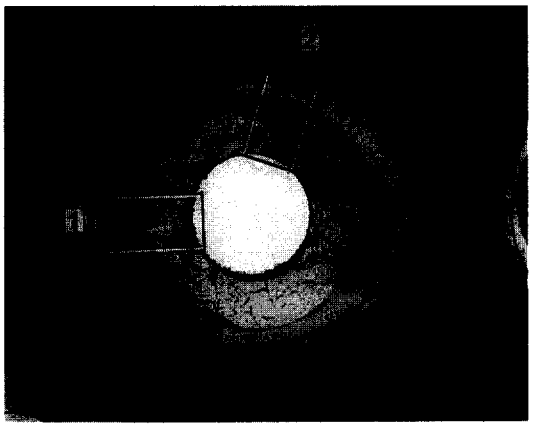

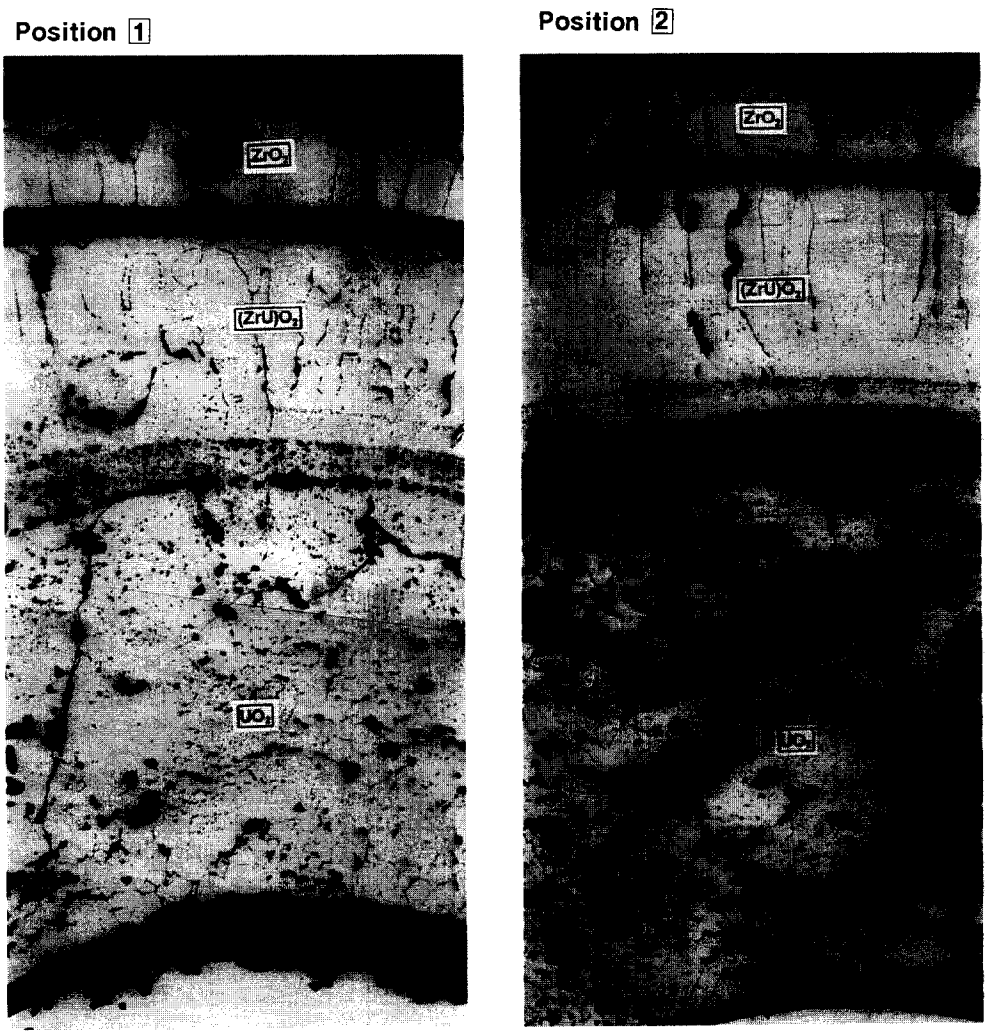

Fig. 2. Cross-section W2-06 of the CORA-W2 test bundle (elevation 726 mm) (from Ref. [10]).

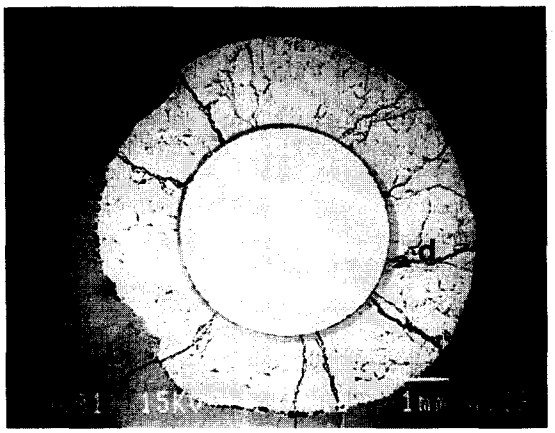

Fig. 3. Cross-section #p, position No. 1 of the CORA-W2 test bundle (elevation 910 mm) (from Ref. [10]).

Fig. 4. Cross-section No. 9, position 6 of the CORA-16 test bundle (elevation 525 mm) (from Ref. [11]).

ent elevations performed in different laboratories [10] evidenced a rather homogeneous composition of (U, Zr)O_{2-x} ceramic layers located between partially dissolved UO_2 pellets and ZrO_2 scales. For example, the results of point analysis of a rod cross-section at elevation 910 mm in the CORA-W2 test performed by the SEM/EDX method at different positions a, b and c (Fig. 3), are collected in Table 1 and demonstrate that within the accuracy limits of the measurements the composition of the ceramic phase is rather homogeneous (6–8 at.% U, 25–28 at.% Zr) and can be fairly represented by the chemical formula $\approx (U_{0.21}Zr_{0.79})O_{2-x}$.

At lower elevations analogous observations of the homogeneous ceramic phase with slightly different compositions were performed: $\approx (U_{0.23}Zr_{0.77})O_{2-x}$ at 607 mm in the CORA-W2 test (see point 1.2 in fig. 9 on p. 87 in Ref. [10]), $\approx (U_{0.12}Zr_{0.88})O_{2-x}$ at 392 mm in the CORA-W2 test (see fig. 20 on p. 208 in Ref. [10] and the more detailed fig. 21 on p. 209 in Ref. [10] (point 4) and fig. 24 on p. 212 in Ref. [10] (point 4)) and $\approx (U_{0.08}Zr_{0.92})O_{2-x}$ at 389 mm in the CORA-W1 test (see fig. 148 in Ref. [8], point 4). A similar result was obtained earlier in the CORA-16 test [11] at 525 mm elevation: $\approx (U_{0.23}Zr_{0.77})O_{2-x}$ (see points 2 and 3 in Fig. 4 and Table 2). In particular, these observations prove the absence of any noticeable U and Zr concentration profiles in radial direction inside the ceramic phase (perhaps, with the exception of thin boundary layers), thus, indirectly confirming a general conclusion (deduced in Ref. [2] on the basis of crucible experiments) about the dominance of convective mixing of the molten phase in the course of the dissolution process also in the rod geometry.

Table 1
Quantitative results of SEM/EDX analysis of material chemical composition at different locations at elevation 910 mm (position No. 1 of cross section #p, Fig. 3) of the CORA-W2 test bundle (from Ref. [10], fig. 72 on p. 261, fig. 73 on p. 262 and fig. 74 on p. 263)

Element (at.%)	Location a (point 3)	Location b	Location e
O	66.3	66.1	65.3
Zr	27.4	25.4	27.5
U	6.3	8.5	7.3

3. Theoretical model

As in Ref. [2], the analytical consideration can be restricted with sufficient accuracy to a one-dimensional problem, due to a small h/R ratio ≤ 0.1 (h is the thickness of the molten part of the Zr cladding and R is the radius of the rod). In the numerical model this restriction can be easily avoided.

3.1. Saturation stage

Rapid saturation of the liquid phase by U, Zr and O atoms due to simultaneous dissolution of UO_2 and ZrO_2 takes place during the saturation period. Under conditions of convective mixing of the liquid phase (sustained also in the rod geometry due to a large weight difference amongst U, Zr and O atoms, as explained in Ref. [2]), the basic equations derived in Refs. [1,2] for the simplified case can

Table 2
Quantitative results of SEM/EDX analysis of material chemical composition at different locations at elevation 525 mm (Fig. 4) of the CORA-W2 test bundle (from [11])

Element (at.%)	Location 1	Location 2	Location 3	Location 4
O	65	65	66	67
Zr	35	27	26.5	0
U	0.3	8	7.5	33

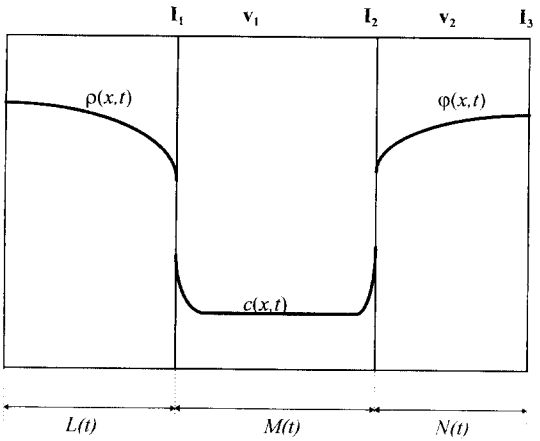

Fig. 5. Schematic representation of the three-layer interaction system.

be easily generalized for the description of simultaneous dissolution of UO_2 and ZrO_2. In the quasi one-dimensional geometry (see Fig. 5), mass balances of the different components (O, U, Zr) in the liquid phase take the form

$$-D_O^{(UO_2)}\partial\rho_O/\partial x|_{I_1} - \rho_O(I_1)\partial L/\partial t + D_O^{(ZrO_2)}\partial\varphi_O/\partial x|_{I_2} - \varphi_O(I_2)\partial N/\partial t = \partial/\partial t[c_O(B)M], \quad (1)$$

$$-\rho_U(B)\partial L/\partial t = \partial/\partial t[c_U(B)M], \quad (2)$$

$$-\varphi_{Zr}(B)\partial N/\partial t = \partial/\partial t[c_{Zr}(B)M], \quad (3)$$

where $c_i(I_{1,2})$, $c_i(B)$ are the molar densities of the different components (i = O, U, Zr) at the interface boundaries ($I_{1,2}$) and in the bulk (B) of the liquid phase, respectively; $\rho_i(I_1)$, $\rho_i(B)$ are the corresponding values in the UO_2 phase; $\varphi_i(I_2)$, $\varphi_i(B)$ are the corresponding values in the ZrO_2 phase; $D_O^{(UO_2)}$, $D_O^{(ZrO_2)}$ are the chemical diffusion coefficients of oxygen in the solid phases.

Flux matches at the two interfaces I_1 and I_2, correspondingly, take the form

$$-\rho_O(I_1)\partial L/\partial t - D_O^{(UO_2)}\partial\rho_O/\partial x|_{I_1} = k_O[c_O(I_1) - c_O(B)] + c_O(B)(v_1 - \partial L/\partial t), \quad (4)$$

$$-\rho_U(B)\partial L/\partial t = k_U[c_U(I_1) - c_U(B)] + c_U(B)(v_1 - \partial L/\partial t), \quad (5)$$

$$-\rho_U(B)\partial L/\partial t = c_M(B)(v_1 - \partial L/\partial t), \quad (6)$$

and

$$\varphi_O(I_2)[v_2 - \partial(L+M)/\partial t] - D_O^{(ZrO_2)}\partial\varphi_O/\partial x|_{I_2} = -k_O[c_O(I_2) - c_O(B)] + c_O(B)[v_1 - \partial(L+M)/\partial t], \quad (7)$$

$$-k_U[c_U(I_2) - c_U(B)] + c_U(B)[v_1 - \partial(L+M)/\partial t] = 0, \quad (8)$$

$$\varphi_U(B)[v_2 - \partial(L+M)/\partial t] = c_M(B)[v_1 - \partial(L+M)/\partial t], \quad (9)$$

where k_O, k_U are convective mass transfer coefficients of O and U atoms in the melt; v_1, v_2 are relative velocities (with respect to the UO_2 layer) of the liquid and ZrO_2 layers, respectively, due to density differences between adjacent phases.

An additional equation

$$v_2 = \partial(L+M+N)/\partial t, \quad (10)$$

which has a clear physical sense can be easily derived from the system of equations, Eqs. (2), (3) and (6).

The system of equations, Eqs. (1)–(9), should be generally completed by the flux match condition at the ZrO_2/steam boundary I_3 for the description of the oxidation process (and corresponding growth of ZrO_2 layer competitive to the dissolution process). Such a general approach will be applied for the development of a numerical model presented in Sections 4 and 5.

In accordance with the equilibrium ternary phase diagram, the liquidus line is approximated at $T = 2000$°C by a linear relationship (compare with Ref. [2]):

$$c_O(I)/(c_O(I) + c_U(I) + c_{Zr}(I)) = -0.45c_U(I)/(c_O(I) + c_U(I) + c_{Zr}(I)) + 0.45. \quad (11)$$

The molar density of pure liquid U is ≈ 0.071 mol/cm^3 and of liquid Zr is ≈ 0.062 mol/cm^3, thus (as in Ref. [2]) it is assumed that the molar density of the melt is independent of the U/Zr ratio:

$$c_U + c_{Zr} + \theta c_O = \text{constant} = c_M \approx 0.068 \text{ mol/cm}^3, \quad (12)$$

where $0 \le \theta \le 1$. In the limiting case $\theta = 1$ the molar density of the melt is independent of its composition and is denoted by c_M. In the other limiting case $\theta = 0$ the molar density of the melt is independent of the dissolved oxygen concentration and is denoted by c_M on an oxygen-free basis. In accordance with the results of validation of the UO_2 dissolution model [2], the best fit of calculations with measurements was attained for $\theta = 0$; therefore, in the present model this assumption is used. For these reasons, Eqs. (6) and (9) which correspond to the sums of flux matches for U and Zr components at the interface take an especially simple form since, under the condition $c_U + c_{Zr}$ = constant, the sum of the convective fluxes of these two components automatically turns to zero (compare with analogous consideration of the diffusion problem by Darken):

$$\rho_O(B) \approx \varphi_O(B) \approx 0.094 \text{ mol/cm}^3,$$

$$\rho_U(B) \approx \varphi_U(B) \approx 0.047 \text{ mol/cm}^3,$$

$$\rho_O(I) \approx \varphi_O(I) \approx 0.087 \text{ mol/cm}^3. \quad (13)$$

Here a simplified feature of the phase diagram is used, where the solidus line can be well approximated by a straight line with a constant content of oxygen $x \approx$ constant in the (U, Zr)O_{2-x} phase [2].

For the qualitative analysis of the complicated behavior of the UO_2/(molten Zr)/ZrO_2 system which can be performed on the basis of analytical consideration, a further simplification of Eqs. (1)–(9) can be obtained using the following additional assumptions for the considered case.

(1) The ZrO_2 scale is considered as a semi-infinite layer, i.e. rather thick in comparison with the characteristic oxygen diffusion length in the solid phase, $[D_O^{(ZrO_2)}t]^{1/2}$.

(2) $c_O(B) = c_U(B) = 0$, at $t = 0$, i.e. oxygen-free molten Zr is considered in the beginning of the dissolution process.

(3) Surface to volume ratio, $A = S/V_{Zr}$, of the molten Zr layer is small in comparison with the inverse characteristic oxygen diffusion length in the solid phase, $[D_O^{(UO_2)}t]^{-1/2}$, during the saturation stage; thus, diffusion oxygen fluxes in the solid UO_2 and ZrO_2 phases can be neglected in the mass balance and flux match equations, Eqs. (1)–(9) (perhaps, with the exception of a relatively short time interval in the end of the saturation stage, see Ref. [2]).

(4) $k_O \approx k_U \approx k$, since this assumption does not strongly influence the final results of calculations (see Refs. [1,2]).

These assumptions restrict the consideration by rather particular (but, generally speaking, realistic) conditions, however, they allow analytical calculations to be performed and on this basis some qualitative conclusions on the system behavior in more general cases (described further quantitatively by the numerical model).

Combining the simplified equations of the above system of equations, Eqs. (1)–(9), and substituting numerical values from Eqs. (11)–(13), a simple differential equation can be derived after some cumbersome but straightforward calculations:

$$\partial L/\partial t\left[2\rho_O M_0/M + (1.6\rho_U/1.5)(L - L_0)/M\right] + 0.8\rho_U = \partial M/\partial t\left[1.5\rho_O M_0/M + 0.8\rho_U(L - L_0)/M\right], \quad (14)$$

where $\rho_O \equiv \rho_O(I_1)$, $\rho_U \equiv \rho_U(B)$, $M_0 = M|_{t=0}$ and $L_0 = L|_{t=0}$.

The solution of Eq. (14) yields a simple relation between the values M and L:

$$M \approx 11.5\left(M_0^2/L^*\right) - (2/3)L^*, \quad (15)$$

where $L^* = L_1 - L_0$, $L_1 = L + (1.5\rho_O/0.8\ \rho_U)M_0$.

Substituting Eq. (15) into Eq. (14), a final solution for $L(t)$ can be found:

$$L - L_0 \approx -0.3M_0\left[1 + 1/\left(\exp(kt/0.76M_0) - 0.05\right)\right]. \quad (16)$$

From this equation a characteristic time t^* of the saturation stage duration can be estimated:

$$t^* \sim 0.76M_0/k, \quad (17)$$

which is approximately two times shorter than the characteristic time of the saturation stage in the absence of the ZrO_2 layer (i.e. the solution of the corresponding problem in Ref. [2] for $\theta = 0$), $t^* \sim 1.4M_0/k$. At large times, $t \gg t^*$, reduction of the UO_2 layer

$$L - L_0 \approx -0.3M_0, \quad (18)$$

is also approximately two times smaller than in the absence of ZrO_2 layer ($L - L_0 \approx -0.6M_0$). Variation of the molten Zr and solid ZrO_2 layers in the end of the saturation stage can be estimated using Eq. (15) on the basis of simple relations between the three values L, M and N, derived from Eqs. (2) and (3):

$$\partial M/\partial t = -(\rho_U/c_M)\partial/\partial t(L + N),$$

resulting in

$$M - M_0 \approx 0.5M_0,$$

$$N - N_0 \approx -0.5M_0. \quad (19)$$

Therefore, the reduction of the ZrO_2 layer is approximately 1.7 times larger than that of the UO_2 layer.

On the basis of these results, a general qualitative conclusion about the strong influence of the ZrO_2 layer on the dissolution kinetics of UO_2 and the amount of dissolved UO_2 in the first, saturation stage could be made. It is also clear that an additional oxygen flux into the molten phase connected with the simultaneous oxidation of Zr in the steam atmosphere will further influence the progression of the dissolution process.

3.2. Precipitation stage

As explained in Ref. [2], during the saturation period the liquid phase reaches saturation, corresponding to a certain point on the liquidus line. With the lack of an equilibrium between the bulk of each solid phase (UO_2 and ZrO_2) and the saturated liquid phase (U, Zr, O), finite gradients of oxygen concentration in the solid phases and oxygen fluxes into the liquid phase are sustained, leading to an oversaturation of the liquid and the precipitation of the solid ceramic phase (U, Zr)O_{2-x}. Simultaneously, the dissolution of solid UO_2 and ZrO_2 is continued but the kinetics of this process changes its character. This stage can be described by the propagation of a 'diffusion path' through the two-phase area in the equilibrium phase diagram and a quantitative theory should include a self-consistent description of the three processes: (1) dissolution of UO_2 and ZrO_2 by the liquid phase; (2) formation (due to precipitation and/or solid phase boundary layer disintegration) and growing of the (U, Zr)O_{2-x} phase (i.e. appearance of a spatial two-phase region) and (3) diffusion transport of oxygen from UO_2 and ZrO_2 to the liquid phase. The final product of these material interaction processes is the three-layer structure UO_2/(U, Zr)O_{2-x}/ZrO_2

observed in the CORA tests (see Section 2). The intermediate layer was apparently formed after the completion of the ceramic (U, Zr)O_{2-x} precipitates formation and growth and had a rather homogeneous composition in all studied cross-sections of the rods (see Section 2).

For the theoretical description of the precipitation stage the model proposed in Refs. [1,2] for the UO_2 dissolution process can be naturally generalized to account for simultaneous dissolution of the ZrO_2 layer. In this case the system of mass balance equations of various elements (O, U, Zr) in the homogeneously mixed liquid phase (containing ceramic precipitates) takes the following form:

$$-\rho_O(I_1)\partial L/\partial t - \varphi_O(I_2)\partial N/\partial t - D_O^{(UO_2)}\partial\rho_O/\partial x|_{I_1} + D_O^{(ZrO_2)}\partial\varphi_O/\partial x|_{I_2} = \partial/\partial t\left[c_O(M-V)\right] + \rho_O(I_1)\partial V/\partial t, \quad (20)$$

$$-\rho_U\partial L/\partial t = \partial/\partial t\left[c_U(M-V)\right] + \partial/\partial t\left[\rho_U(1-\alpha)V\right], \quad (21)$$

$$-\rho_U\partial N/\partial t = \partial/\partial t\left[c_{Zr}(M-V)\right] + \partial/\partial t(\rho_U\alpha V), \quad (22)$$

where parameter α describes the ceramic precipitate $(U_{1-\alpha}, Zr_\alpha)O_{2-x}$ composition, and V is defined as the integral volume of this precipitated phase divided by the solid/liquid interface area.

The system of equations, Eqs. (20)–(22), is incomplete for self-consistent description of the dissolution process since it describes only conservation laws (mass balances). For this reason it should be generally completed by flux match conditions at the solid/liquid interfaces. However, the formation of the two-phase zone (liquid + ceramic precipitates) near the interface makes this problem especially complicated. Instead of flux match equations, it was suggested in Refs. [1,2] to use additional simple assumptions based on the experimental observations which allowed the solution of the incomplete system of mass balance equations, Eqs. (20)–(22). In Refs. [1,2] such an assumption was $\alpha \approx$ constant, which corresponds to the invariable composition of the ceramic phase $(U_{1-\alpha}, Zr_\alpha)O_{2-x}$ formed during the precipitation stage. This assumption was in fair agreement with direct observations of various crucible tests.

In the presently considered case of simultaneous dissolution of UO_2 and ZrO_2 such an assumption can be confirmed indirectly. Indeed, as explained above, the chemical composition of the formed (U, Zr)O_{2-x} ceramic layer was rather homogeneous in various cross-sections of the rods studied in the post-test CORA examinations. Taking into account extremely small values of U and Zr atoms diffusion coefficients in the ceramic phase ($\approx$ five orders of magnitude smaller than that of O atoms), the observed homogeneous distribution of U and Zr atoms in the solid (U, Zr)O_{2-x} ceramic layer can be explained only in one way. Namely it should be assumed that the ceramic precipitates, which appeared and grew up at various locations and times of the precipitation stage, initially had the same composition, i.e. $\alpha(x, t) \approx$ constant.

In the case of only one (UO_2) layer dissolution [1,2] this additional assumption was enough for the solution of the problem. In the case of the two layer (UO_2 and ZrO_2) dissolution, one more additional assumption must be used. This new assumption concerning the behavior of the UO_2/liquid interface boundary can be made on the basis of further analysis of the UO_2 crucible tests. As discussed in Refs. [1,2], the UO_2 dissolution rates during the precipitation stage in the tests with large value of $A = S/V_{Zr} \approx 10^{-15}$ cm^{-1} (namely experiments [4]) characteristic for the rod geometry, were negligibly small at 1900–2000°C increasing at higher temperatures. However, even at higher temperatures an addition of a relatively small (≈ 6 wt%) portion of oxygen into the Zr melt suppressed significantly the UO_2 dissolution rates at the precipitation stage (see figs. 8 and 9 in Ref. [4]).

On the basis of these observations it is logical to propose that in the case of an additional oxygen flux into the molten Zr from the ZrO_2 phase which provides comparable amounts of oxygen in the melt after cessation of the first saturation stage and its further increase in the steam atmosphere, that the UO_2 dissolution process will be also strongly suppressed at the precipitation stage in the considered geometry at all temperatures of interest.

On the basis of these two additional assumptions, $\alpha \approx$ constant and $\partial L/\partial t \to 0$, the solution of the system of equations, Eqs. (20)–(22), can be unambiguously derived:

$$\partial V/\partial t = -(\partial N/\partial t)c_U/\left[c_U - (1-\alpha)c_M\right], \quad (23)$$

$$\partial M/\partial t = -(\partial N/\partial t)\left[c_U - \rho_U(1-\alpha)\right]/\left[c_U - (1-\alpha)c_M\right], \quad (24)$$

$$\partial N/\partial t = (J_1 - J_2)\left[1 - c_U/(1-\alpha)c_M\right]/\left[\rho_O - \rho_U c_O/c_M\right], \quad (25)$$

where $J_1 \equiv -D_O^{(UO_2)}\partial\rho_O/\partial x|_{I_1}$, $J_2 \equiv -D_O^{(ZrO_2)}\partial\varphi_O/\partial x|_{I_2}$. From analysis of Eqs. (23)–(25) it is clearly seen that the amount of the precipitated phase always increases with time during the precipitation stage, since

$$\partial V/\partial t = (J_1 - J_2)\left[c_U/(1-\alpha)(c_M\rho_O - c_O\rho_U)\right] > 0,$$

independent of the numeric value of the parameter $\alpha < 1$.

On the other hand, this parameter α significantly influences the behavior of the ZrO_2 layer, since $\partial N/\partial t > 0$ in the case $\alpha < 1 - c_U/c_M$ (i.e. corrosion) and $\partial N/\partial t < 0$ in the case $\alpha > 1 - c_U/c_M$ (i.e. erosion). Therefore, a critical value $\alpha^* = 1 - c_U/c_M$, determines the boundary between two different regimes of the ZrO_2 layer behavior in the precipitation stage: growth or dissolution.

Calculations, by the numerical model presented below, demonstrate that in the case of simultaneous dissolution (UO_2/(molten Zr)/ZrO_2), the ratio c_U/c_M becomes small in the end of the saturation stage and rather weakly

depends on initial parameters. For example, if the initial ZrO_2 oxide scale thickness H is varied in the range 50 $\mu m < H < 500$ μm, the critical value of the parameter α can be determined as

$$0.85 < \alpha^* < 0.88. \quad (26)$$

Experimental values of the parameter α corresponding to the post-test CORA examinations in various cross-sections of the fuel rod bundle (see Section 2) are in the vicinity of the interval indicated in Eq. (26). This means that both regimes of the ZrO_2 layer behavior (growth and dissolution) could be realized in the CORA tests at various elevations during the second, precipitation stage. In all the cases it can be generally concluded that the ZrO_2 thickness variation was very slow in comparison with that obeyed an ordinary oxidation parabolic kinetics (since α was close to the critical value α^*).

In this situation when the 'protective' oxide layer varies slowly, the oxygen flux (after some initial time interval) practically does not decrease with time, thus, much more oxygen can be consumed by growing ceramic precipitates in the bulk of the liquid phase in comparison with the ordinary oxidation process (when the amount of oxygen consumed by the growing ZrO_2 layer decreases with time obeying parabolic time law). For these reasons, the heat release connected with the oxidation of the melt by formation of (U, Zr)O_{2-x} precipitates can be much higher than in the case of ZrO_2 scale growth obeyed ordinary parabolic time law.

In order to illustrate this conclusion directly, a long term behavior ($t \gg t^*$) of the system can be considered when the composition of the UO_2 phase layer is completely reduced to UO_{2-x} (i.e. no oxygen flux exist from this layer, $J_1 \to 0$) and the finite oxygen concentration drop $\Delta\rho_O$ across the ZrO_2 layer is provided by the stoichiometric oxide composition at the ZrO_2/steam interface, i.e. $J_2 \approx D_O^{(ZrO_2)}\Delta\rho_O/N(t)$. In this case

$$\partial N/\partial t = D_O^{(ZrO_2)}\Delta\rho_O[1 - c_U/(1-\alpha)c_M]/N(t)[\rho_O - \rho_U c_O/c_M],$$

or

$$(1/2)\partial N^2/\partial t = D_O^{(ZrO_2)}\Delta\rho_O[1 - c_U/(1-\alpha)c_M]/[\rho_O - \rho_U c_O/c_M] = J^*[1 - c_U/(1-\alpha)c_M],$$

where J^* characterizes the oxidation rates $(1/2)\partial N^2/\partial t$ of the melt in the ordinary case, i.e. without precipitation inside the melt. From this equation it is clearly seen that at $\alpha \to \alpha^*$, variation of the oxide layer thickness $N(t)$ becomes slow in comparison with the ordinary oxidation kinetics. On the other hand, $\partial V/\partial t \gg \partial N/\partial t$ in this case, which means that practically all oxygen is consumed by growing (U, Zr)O_{2-x} precipitates inside the melt. The total volume of the oxide phases (ZrO_2 and (U, Zr)O_{2-x}) formed under these conditions is determined by the same expression as in the ordinary case (with only one oxide phase ZrO_2): $\partial V/\partial t + \partial N/\partial t = J^*/N(t)$, but with a much slower variation of $N(t)$ on the right hand side of this expression. Finally, it leads to the above-derived conclusion about significant increase of oxygen consumption in the course of the oxide phases growth. In particular, it proves that heat release connected with oxidation of the melt by formation and growth of the (U, Zr)O_{2-x} precipitates is much higher than in the case of an ordinary ZrO_2 scale growth obeyed parabolic time law.

4. Numerical model

For the description of a general case of simultaneous dissolution of the UO_2 pellet and the ZrO_2 layer in an oxidizing atmosphere, without simplifying assumptions accepted in Section 3, a numerical model is developed based on the general solution of Eqs. (1)–(9) and the oxygen solid state diffusion problem.

In order to calculate the oxygen diffusion fluxes in Eqs. (1), (4), (7) and (25), oxygen concentration distributions in the UO_2 pellet and in the ZrO_2 scale are searched by the solution of diffusion equations

$$\frac{\partial c}{\partial t} + v^{(i)}\frac{\partial c}{\partial x} = D_O^{(i)}\frac{\partial^2 c}{\partial x^2}, \quad (27)$$

where $v^{(i)}$ and $D_O^{(i)}$ are convective velocity and diffusion coefficient of the corresponding layer ($i = UO_2$, ZrO_2), respectively. Boundary conditions take form

$$\left.\frac{\partial c}{\partial x}\right|_{x=0} = 0; \quad c(x = x_1(t), t) = \rho_O(I_1), \quad (28)$$

for the UO_2 layer and

$$c(x = x_2(t), t) = \varphi_O(I_2); \quad c(x = x_3(t), t) = \varphi_O(B) \quad (29)$$

for the ZrO_2 layer under unlimited steam supply conditions. Interface positions $x_1(UO_2/melt)$, $x_2(melt/ZrO_2)$ and $x_3(ZrO_2/steam)$ are simply connected with the already introduced layer thicknesses: $x_1 = L$, $x_2 = L + M$, $x_3 = L + M + N$ (see Fig. 5).

Direct numerical solution of the diffusion equation, Eq. (27), in a region with moving boundaries is a rather complicated problem, which requires consideration of adaptive mesh grids and corresponding approximation procedures providing implementation of conservation laws. However, the problem becomes more simple in a new coordinate system connected with moving boundaries [12].

Indeed, by means of a coordinate transformation $q = x/x_1(t)$ for the UO_2 layer, Eq. (27), and the boundary conditions, Eq. (28), are reduced to the form

$$\frac{\partial c}{\partial t} - \frac{q}{x_1}\frac{dx_1}{dt}\frac{\partial c}{\partial q} = \frac{D_O^{(UO_2)}}{x_1^2}\frac{\partial^2 c}{\partial q^2}, \quad \left.\frac{\partial c}{\partial q}\right|_{q=0};$$

$$c(q = 1, t) = \rho_O(I_1). \quad (30)$$

Analogously, a coordinate transformation $q = (x - x_2)/(x_3 - x_2)$ for the ZrO_2 layer in Eqs. (27) and (29) leads to

$$\frac{\partial c}{\partial t} - \frac{v_2 - \mathrm{d}x_2/\mathrm{d}t - q(\mathrm{d}x_3/\mathrm{d}t - \mathrm{d}x_2/\mathrm{d}t)}{x_3 - x_2} = \frac{D_O^{(UO_2)}}{x_1^2}\frac{\partial^2 c}{\partial q^2}, \quad c(q=0,t) = \varphi_O(I_2); \quad c(q=1,t) = \varphi_O(B). \tag{31}$$

After such coordinate transformations additional convective terms appeared in the diffusion equations, which should be solved, however, in a fixed boundary region.

Consideration of diffusion processes in the UO_2 and ZrO_2 layers requires the determination of corresponding oxygen solid state diffusion coefficients. At temperatures above 1773 K the oxide scale consists of an outer tetragonal layer and an inner cubic oxide scale. In Ref. [13], to simplify the in-reactor corrosion analyses, the duplex scale was represented by a single homogenized oxide layer and a single effective diffusion coefficient was determined on the basis of the available experimental oxidation kinetics data. According to the recommendations of Ref. [13], the effective coefficient $D_O^{(ZrO_2)} = 20\exp(-2400/T\ (\mathrm{K}))$ cm^2/s and the value of the O/Zr ratio at the oxide lower phase boundary 1.72 were used in the numerical calculations. Using the critical evaluation of the experimental data on measurements of the oxygen diffusivity in the solid UO_2 phase [2], the chemical diffusion coefficient of oxygen in the solid UO_2 phase $D_O^{(UO_2)} = 5 \times 10^{-4}$ cm^2/s was taken at $T = 2000°C$.

The initial oxygen distributions in the solid phases and the ZrO_2 scale thickness are determined by the oxidation processes taking place in the course of temperature escalation up to the α-Zr(O) melting point and could be found from numerical solution of the cladding oxidation problem. Since such a detailed consideration of the temperature escalation stage is beyond the scope of the present paper, the initial ZrO_2 layer thickness was varied in a wide interval approximately corresponding to the post-test observations of the CORA tests. For the sake of simplicity, the initial oxygen concentration profiles are assumed to be linear in the ZrO_2 layer and constant (corresponding to the stoichiometric composition) in the UO_2 pellet, with the exception of a narrow band of about 100 μm thickness near the boundary, where the oxygen concentration smoothly reduces to the value $\rho_0(I_1)$.

For the numerical solution of Eqs. (30) and (31) an implicit difference scheme was developed. The obtained boundary-value problem for the second order difference equations was solved by the elimination method [14]. The desired calculation accuracy was attained by the selection of an adaptive integration time step. The general algorithm of the self-consistent solution of Eqs. (1)–(9), (30) and (31) was as follows: the initial oxygen concentration distributions in the UO_2 and the ZrO_2 layers enable to solve Eqs. (1)–(9) at one time integration step and calculate boundary displacement and necessary velocities $\mathrm{d}x_i/\mathrm{d}t$, v_i; after this, new oxygen concentration distributions are found by solving Eqs. (30) and (31) and so on. The liquid phase saturation is reached when $C_U(I_1) = C_U(B)$ and, thus, the uranium concentration gradient in the melt vanishes. At the precipitation stage, Eqs. (1)–(9) are substituted by Eqs. (23)–(25) retaining the described calculation flow.

The above presented model was also extended to the case of a fuel rod geometry. Generalization of Eqs. (1)–(9), (23)–(25), (30) and (31) for cylindrical symmetry geometry is straightforward and its description is omitted here.

5. Numerical results

In this section results of numerical calculations by the developed model are presented. At first, two important particular cases are considered. Analysis of the general situation is presented in Section 5.3.

5.1. Simultaneous dissolution in the case of small oxygen diffusion fluxes

In Section 3.1 the analytical solution of the problem of simultaneous dissolution of the UO_2 and ZrO_2 slabs by molten Zr was obtained for the limiting case, when oxygen diffusion fluxes in the solid phases can be neglected (i.e. small S/V_{Zr} ratio). This case gives a reference point, allowing the importance of solid state oxygen diffusion in dissolution kinetics to be judged and enables a close approximation for the behavior of the UO_2/(molten Zr)/ZrO_2 system under various realistic conditions. For this reason, some numerical calculations of Eqs. (1)–(9) modified for the case of a cylindrical geometry with the natural-convection mass transfer coefficients $k_O = 10^{-2}$ cm^2/s, $k_U = 5 \times 10^{-3}$ cm^2/s and zero solid state oxygen diffusivities $D_O^{(UO_2)} = D_O^{(ZrO_2)} = 0$ are carried out.

The initial fuel rod geometry was as follows: UO_2 pellet radius, $r_1^0 = 0.5$ cm; outer melt radius, $r_2^0 = 0.6$ cm and outer ZrO_2 oxide scale radius, $r_3^0 = 1$ cm. At the end of the saturation stage, radius variations corresponding to the values L, M, N introduced earlier in the case of a plane geometry were obtained: $r_1 - r_1^0 = -0.275(r_2^0 - r_1^0)$, $r_2 - r_1 = r_2^0 - r_1^0 + 0.6(r_2^0 - r_1^0)$ and $r_3 - r_2 = r_3^0 - r_2^0 - 0.6(r_2^0 - r_1^0)$.

During the saturation stage, the system follows the trajectory OP′ in Fig. 6. Recall that in the case of UO_2/(molten Zr) interactions the trajectory in Fig. 6 follows the material balance tie-line connecting the Zr corner with the point representing UO_2. In the case under consideration the trajectory is considerably shifted towards lower uranium contents, this is connected with essential ZrO_2 dissolution rate. In the end of the saturation stage the

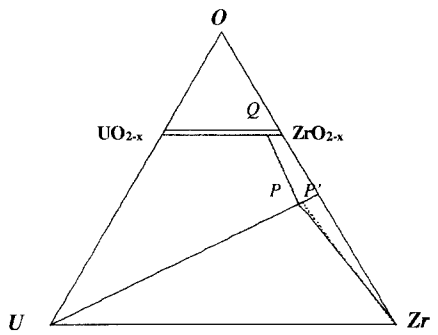

Fig. 6. Schematic representation of the equilibrium ternary phase diagram at $T = 2000$°C and calculated phase trajectories. Points P and P′ on the liquidus line correspond to the phase trajectories during the saturation stage with zero and nonzero solid state oxygen diffusivities, respectively; material balance tie line PQ represents the phase trajectory during the precipitation stage.

O/Zr atomic ratio in the liquid phase was calculated to be about 0.6 (point P′ in Fig. 6). This means that the ZrO_2 oxide scale is dissolved by molten Zr about two times faster than UO_2. The reason of this substantial distinction can be illustrated by the following consideration. As follows from Eqs. (4), (5), (8) and (11), at $t = 0$ the interface concentrations are approximately equal to $C_O(I_1) - C_O(B) \approx 0.8 C_M k_U \rho_O(I_1)/(k_U \rho_O(I_1) + 0.8 k_O \rho_U) \approx 0.03$ mol/cm^3 and $C_O(I_2) - C_O(B) \approx 0.8 C_M \approx 0.054$ mol/cm^3 and the ratio between them is kept roughly invariant throughout the saturation period (as can be shown by straightforward calculations). Therefore, the dissolution driving force $C_O(I) - C_O(B)$ at the UO_2/(molten Zr) interface is about two times lower than that at the ZrO_2/(molten Zr) interface. The calculated weight fraction of the UO_2 pellet dissolved during the saturation stage is $\eta \approx 10.5\%$.

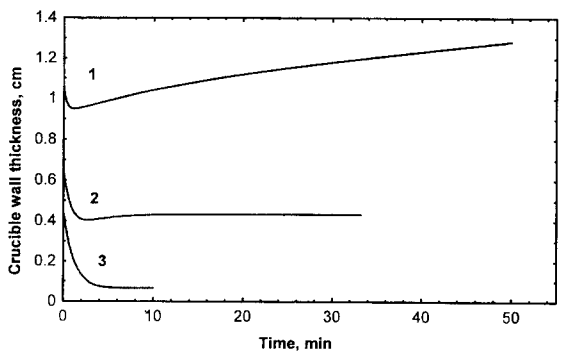

Fig. 7. Interactions of the cylindrical ZrO_2 wall with molten Zr (initial inner radius equals 0.3 cm (curve 1); 0.7 cm (2) and 0.9 cm (3)).

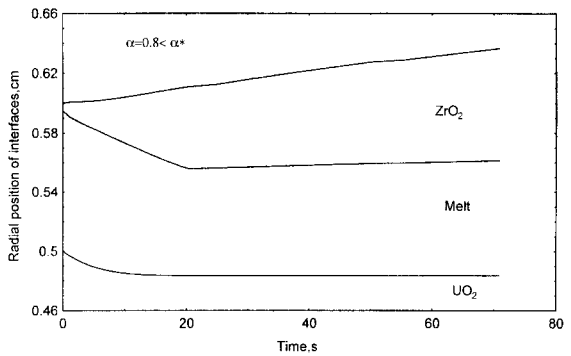

Fig. 8. Movement of the reaction layer interfaces in the case of a thin initial ZrO_2 oxide scale, $H = 50$ μm $< H^*$.

5.2. Dissolution of ZrO_2 by molten Zr

Another particular case which can be described by the general model is the dissolution of the ZrO_2 scale by molten Zr in an inert atmosphere in the absence of interactions with UO_2. Such a consideration is important for the study of the oxide scale mechanical rupture under conditions of a severe accident and can be applied to the description of separate-effect tests on the ZrO_2 crucible dissolution by molten Zr.

For better understanding of the interaction kinetics two limiting cases have been considered. In the first limiting case, the ZrO_2 walls are much thicker than the molten Zr radius. In this case, during relatively short erosion period the oxygen concentration in the liquid phase reaches its equilibrium value. However, by the end of this period ZrO_2 walls contain considerable amount of excessive oxygen in comparison with its equilibrium value. Relaxation of this non-equilibrium state by the oxygen diffusion in the solid state leads to the inward movement of the oxide/melt boundary to the center of the molten phase. The duration of this stage is determined by the characteristic oxygen solid state diffusion time. This case is illustrated by numer-

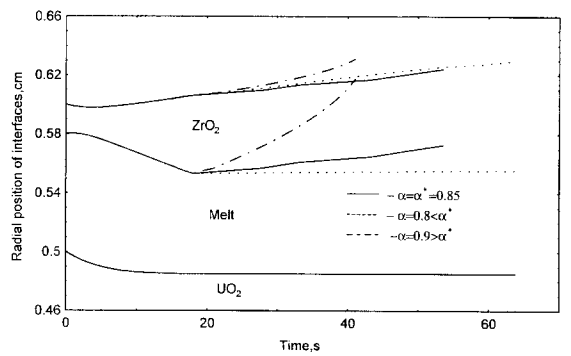

Fig. 9. Movement of the reaction layer interfaces in the case of a thick initial ZrO_2 oxide scale, $H = 200$ μm $> H^*$ for various precipitate compositions.

ical calculations in Fig. 7 (curve 1). In the opposite limiting case, when the ZrO_2 wall thickness is much smaller than melt radius, all excessive oxygen in the ZrO_2 transfers into the melt during the erosion period. Therefore, interactions cease after completion of the erosion process. This case is represented in Fig. 7 by curve 3. An intermediate case of close linear dimensions of the two phases is represented in the same figure by curve 2.

5.3. General case of simultaneous UO_2 and ZrO_2 dissolution by molten Zr in oxidizing atmosphere

In what follows, calculation results will be discussed obtained by the complete numerical model based on Eqs. (30) and (31) and Eqs. (1)–(9) or Eqs. (23)–(25). An important parameter determining the kinetics of the ZrO_2 oxide scale growth is its initial thickness $H = r_3^0 - r_2^0$. Indeed, in the case of a small initial thickness of the oxide scale $H \ll H^* \simeq D_O^{(ZrO_2)}\Delta\rho_0/(0.8k_OC_M) \approx 130$ μm the oxygen diffusion flux through the ZrO_2 layer $F_d \simeq D_O^{(ZrO_2)}\Delta\rho_0/H$ is much larger than the oxygen convective flux in the liquid phase at the liquid/ZrO_2 interface $F_c \simeq k_O(C_O(I_2) - C_O(B))$. This results in increasing of the ZrO_2 scale thickness. In the opposite limiting case $H \gg H^*$ molten Zr dissolves the oxide in the beginning of the saturation stage. At the end of this stage when saturation of the liquid phase is approached, the convective flux F_c considerably diminishes and the oxygen solid state diffusion causes an increase of the ZrO_2 layer thickness. This qualitative consideration is confirmed by the numerical calculations presented in Figs. 8 and 9.

The above described situation drastically changes under steam starvation conditions. The ZrO_2 oxide scale with initial thickness $\Delta_0 \simeq 100$ μm is dissolved completely within a few seconds. The time of complete external oxide dissolution could be roughly estimated as: $\tau \simeq \Delta_0\rho_O(I_2)/k_OC_O(I_2) \approx 2$s.

An interesting feature of the cladding growth dynamics is that for the initial ZrO_2 layer thickness varying in a wide range $0 < r_3^O - r_2^O < 500$ μm the final ZrO_2 oxide scale thickness attained in the end of the saturation stage is practically invariant ≈ 530 μm (see Fig. 10).

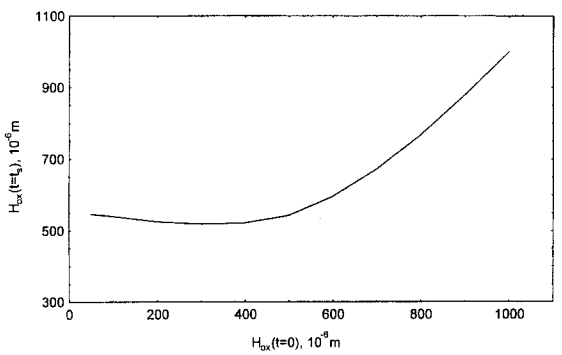

Fig. 10. Thickness of the oxide scale in the end of the saturation stage versus its initial thickness in the case of fixed initial cladding radius 0.6 μm.

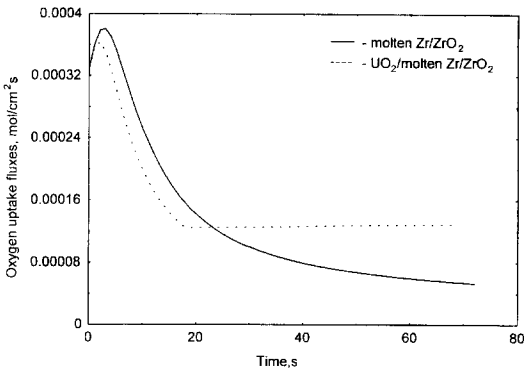

Fig. 11. Oxygen fluxes through the oxide shell.

The trajectory OPQ in Fig. 6 corresponds to the UO_2/(molten Zr)/ZrO_2 system behavior presented in Fig. 9. During the precipitation stage, the system follows the material balance tie line PQ. The indicated point Q is plotted for the parameter $\alpha = \alpha^* \approx 0.855$. As shown in Section 3.2, in the case of $\alpha < \alpha^*$, the ZrO_2 layer thickness enlarges, in the case $\alpha > \alpha^*$, the ZrO_2 layer thickness reduces. This is illustrated in Fig. 9.

An account of the oxygen solid state diffusion processes results in about two times lower value of the dissolved weight fraction of the UO_2 pellet $\eta \approx 5$–6%. This reduction of the dissolved part of the UO_2 pellet may be even more pronounced, if the initial oxygen content in the liquid phase is finite. For example, $\eta \approx 3\%$ if the initial oxygen contents in the liquid phase at the melting point of the cladding corresponds to the linear distribution of the oxygen concentration in the α-Zr(O) layer.

Fig. 11 shows the comparison of cladding oxygen consumption due to oxidation in two cases: when the UO_2/(molten Zr) interaction is taken into account (i.e. double-side simultaneous dissolution by molten Zr of UO_2 and ZrO_2) or not (i.e. one-side dissolution of ZrO_2). In the first case, the ZrO_2 scale does not grow or grows very slowly ($\alpha \approx \alpha^*$) during the precipitation stage, hence, oxygen consumption stabilizes after some initial time intervals (≈ 20 s). In the second case after ≈ 20 s the oxide thickness growth obeys an ordinary parabolic time law and gradually decreases, thus, the oxygen consumption becomes very small in comparison with the first case in the late stage of the process ($t \geq 50$ s). This confirms the qualitative conclusions derived in Section 3.2 about high oxygen consumptions and heat generation connected with oxidation of the melt by formation and growth of the (U, Zr)O_{2-x} precipitates, in comparison with an ordinary case of parabolic ZrO_2 scale growth.

6. Conclusions

The analysis of available metallographic data obtained in the CORA post-test examinations is performed in the present paper. This analysis provides some qualitative and quantitative information concerning physical mechanisms of simultaneous dissolution of UO_2 and ZrO_2 by molten Zr at high temperatures. On this basis a new model describing the dissolution processes and accounting for a competitive process of molten Zr oxidation in the steam environment is developed by generalization of the previously developed model [1,2] of UO_2 dissolution by molten Zr.

Similarly to the simple case of the UO_2 dissolution considered in [1,2], the new model predicts the existence of two stages of the process. During the first, saturation stage molten Zr dissolves the UO_2 and ZrO_2 layers simultaneously and rather quickly reaches saturation. During the second, precipitation stage dissolution of UO_2 is strongly suppressed owing to additional oxygen fluxes into the melt from the ZrO_2 and steam. Competitive processes of the dissolution of ZrO_2 and the oxidation of the Zr melt are accompanied by precipitation of the ceramic $(U_{1-\alpha}, Zr_\alpha)O_{2-x}$ phase. Depending on the composition of the liquid phase attained during the first, saturation stage (and, therefore, on composition α of ceramic precipitates which are in thermodynamic equilibrium with the liquid phase), the competition between dissolution and oxidation processes results in an increase (when $\alpha < \alpha^*$) or decrease (when $\alpha > \alpha^*$) of the ZrO_2 layer thickness. In both the cases variation of the oxide thickness with time is rather slow if the deviation of α from the critical value α^* is small. A comparison of the value α^* calculated by the model with results of point analyses of ceramic precipitates in the CORA post-test examinations at various elevations of the bundle, revealed the above-indicated proximity $\alpha \approx \alpha^*$ practically in all examined cross-sections. This allows qualitative conclusions about the high oxygen consumption and heat generation connected with the oxidation of the melt by the formation and growth of the (U, Zr)O_{2-x} precipitates, in comparison with the ordinary case of ZrO_2 scale growth obeyed parabolic time law.

Numerical calculations by the developed model self-consistently describe the complicated behavior of the UO_2/(molten Zr)/ZrO_2/steam system in both the stages of the process and provide a necessary basis for the consideration of oxidation/dissolution processes in the melt in the course of its downward relocation along the fuel rods, presented in the following part 2 of the paper.

Acknowledgements

The authors are grateful to Dr P. Hofmann and Dr V. Noack (FZK, Karlsruhe) for valuable discussions and comments. We also thank them and Dr S. Hagen (FZK, Karlsruhe) for their kind delivery of the original photographs of samples from the CORA tests. This work was supported by the US Nuclear Regulatory Commission under the NRC Contract No. W6452.

References

[1] M.S. Veshchunov, P. Hofmann, J. Nucl. Mater. 209 (1994) 27.
[2] M.S. Veshchunov, P. Hofmann, A.V. Berdyshev, J. Nucl. Mater. 231 (1996) 1.
[3] P. Hofmann, H. Uetsuka, A.N. Wilhelm, E.A. Garcia, Proc. Int. Symp. on Severe Accidents in Nuclear Power Plants, Sorrento, Italy, 1988, IEAE-SM-296/1, p. 3.
[4] K.T. Kim, D.R. Olander, J. Nucl. Mater. 154 (1988) 102.
[5] P.J. Hayward, I.M. George, J. Nucl. Mater. 208 (1994) 35.
[6] P.J. Hayward, I.M. George, J. Nucl. Mater. 208 (1994) 43.
[7] P. Hofmann, S. Hagen, G. Schanz, A. Skokan, Nucl. Safety 87 (1989) 146.
[8] S. Hagen, P. Hofmann, V. Noack, G. Schanz, G. Schumacher, L. Sepold, Test Results of Experiment CORA W1, Report KfK 5212, 1994.
[9] S. Hagen, P. Hofmann, V. Noack, G. Schanz, G. Schumacher, L. Sepold, Results of Experiment CORA W2, Report KfK 5363, 1994.
[10] L. Sepold (Ed.), Post-test Examination of the VVER-1000 Fuel Rod Bundle CORA-W2, Report FZKA 5570, 1995.
[11] J. Burbach, Ergebnisse von REM/EDX-Mikrobereichsanalysen des Siedewasserreaktor-Buendelabschmelzexperiments CORA-16, Report KfK 5282, 1994.
[12] F.C. Iglesias, D.B. Duncan, S. Sagat, H.E. Sills, J. Nucl. Mater. 130 (1985) 36.
[13] D.R. Olander, Nucl. Eng. Des. 148 (1994) 253.
[14] A.A. Samarskii, E.S. Nicolaev, Numerical Methods for Grid Equations, Birkhaeuser, Basel, 1989.